




Influence of chemically synthesized powder addition on $K_{0.5}Na_{0.5}NbO_3$ ceramic's properties

Emanuele Migliori^{1,2}, Elisa Mercadelli^{1,*} , Ruben Beltrami², Marco Mariani², Carlo Baldisserrri¹, Carmen Galassi^{1,2}, and Nora Lecis²

¹National Research Council of Italy, Institute of Science and Technology for Ceramics, (CNR-ISTEC), Via Granarolo 64, 48018 Faenza, Italy

²Department of Mechanical Engineering, Politecnico di Milano, Via G. La Masa 1, 20156 Milan, Italy

Received: 4 April 2022

Accepted: 29 July 2022

Published online:

30 August 2022

© The Author(s) 2022

ABSTRACT

A new strategy to produce lead-free $K_{0.5}Na_{0.5}NbO_3$ (KNN) piezoceramics with reliable and improved piezoelectric performance is presented for the first time. KNN powders were synthesized using two distinct synthesis routes: a mechanochemical activation-assisted solid-state route (KNN_{SSR}) and a sol-gel modified Pechini method (KNN_{chem}). KNN_{chem} powders were mixed with KNN_{SSR} at different weight ratios (0, 3, 5, 10 and 20 wt%), and the mixtures were conventionally consolidated and sintered at 1130 °C for 2 h. It was found that KNN_{chem} powders influence crystal phase, microstructure and piezoelectric properties of the sintered pellets. Gradually increasing KNN_{chem} content promotes the conversion of the undesired phase present in KNN_{SSR} into the stoichiometric one. It is also proved that the addition of KNN_{chem} between 5 and 10 wt% improves piezoelectric properties, eventually leading to a d_{33} piezoelectric charge constant value of 113–115 pC/N. These values are among the highest reported for undoped KNN ceramics obtained by conventional sintering.

1 Introduction

Potassium Sodium Niobate ($K_{1-x}Na_xNbO_3$, KNN henceforth) is a piezoelectric ceramic material thoroughly studied in the last two decades owing to its promising properties as a possible lead-free alternative to well-known, high-performing lead-based piezoceramic systems such as PZT and PMN [1]. KNN-based piezoceramics show, in fact, interesting

characteristics such as high T_C , good temperature stability of their piezoelectric properties, good mechanical quality factor and fatigue resistance, low density, and biocompatibility [2]. However, pure KNN and KNN-based materials still suffer from reproducibility issues such as volatilization of low-melting Na_2O and K_2O species during calcination or sintering steps, which can detrimentally affect their final stoichiometry [3], chemical inhomogeneities in the calcined powders and sintered samples [4], a very

Address correspondence to E-mail: elisa.mercadelli@istec.cnr.it

narrow sintering temperature range, immediately below its solidus temperature [5], and abnormal grain growth phenomena reported to occur during sintering [6] or even during calcination [7]. Moreover, it was demonstrated in previous works [8, 9] that in undoped $K_{0.5}Na_{0.5}NbO_3$, the final piezoelectric properties are strongly affected by each step of the production process; among these, insufficient milling treatment of the starting powders can lead to chemical composition inhomogeneities in the ceramics, resulting in poor piezoelectric properties.

Nevertheless, the growing need of producing KNN with piezoelectric properties comparable to those of Pb-based materials has motivated the scientific community to pursue two main research lines, both with and without the use of doping elements. On the one hand, the addition of doping elements (e.g., Li, Ta and Sb [10]) and/or the formation of solid solutions with other perovskite compounds (e.g., $Bi_{0.5}Na_{0.5}ZrO_3$, $LiSbO_3$, $BaZrO_3$ etc. [11]) were studied as tools for phase boundaries tuning purposes, or even creating new ones with the aim of increasing the piezoelectric performance [12]. Even though the introduction of dopants generated many novel KNN-based compositions with improved piezoelectric performance [13, 14], issues related to reproducibility and process scalability of such complex compositions still hinder their widespread use in commercial applications.

On the other hand, piezoelectric properties of pure $K_xNa_{1-x}NbO_3$ were improved by using two different approaches: (I) synthesis of starting powders by different methods such as sol–gel precipitation [15–17], hydrothermal [18–20], spray-drying [21] and spray pyrolysis [22], and (II) by exploiting process strategies (i.e., texturing [23–26]) and more effective sintering methods such as spark plasma sintering [20, 27–30], hot pressing [31–33], microwave sintering [34, 35] and liquid-phase sintering [36, 37].

The above-mentioned approach based on alternative synthesis methods can be useful for lowering processing temperatures and thus avoid deviations from the ideal stoichiometry due to alkali evaporation [38] yielding higher piezoelectric performance, as shown by d_{33} values about 150 pC/N [16]. Even though the use of alternative processing or sintering methods provides more effective ways to produce dense KNN ceramics [20, 31], limitations related to longer production times, higher costs and difficult scalability hinder their widespread exploitation.

Therefore, conventional processing and sintering of $K_xNa_{1-x}NbO_3$ having simple compositions remain appealing from an industrial point of view in spite of the lower achievable piezoelectric performance (best d_{33} values about 102–120 pC/N were recently reported [39, 40]).

The aim of this work is to demonstrate for the first time a novel and simple strategy for improving the piezoelectric performance of $K_{0.5}Na_{0.5}NbO_3$ ceramics by means of standard sintering and easy scalable methods, thus avoiding unconventional processes such as texturing, SPS or hot pressing. The concept is based on adding chemically synthesized KNN powder to the one produced via the solid-state reaction route. The use of finer and more reactive nanometre-sized starting powders produced by a sol–gel synthesis route can in fact enhance the driving force of the sintering step [41, 42]. The effect of adding nanosized KNN powder on phase composition, microstructure and piezoelectric properties is thoroughly investigated. This new strategy could be easily transferred to the preparation of a wide range of KNN-based ceramics featuring improved and reliable performances.

2 Material and methods

2.1 KNN powders synthesized via solid-state reaction (KNNSSR)

A mechanochemical activation-assisted solid-state reaction was used to synthesize powders with nominal $K_{0.5}Na_{0.5}NbO_3$ composition. Na_2CO_3 (Merck, purity 99.5%), K_2CO_3 (Merck, purity 99%) and Nb_2O_5 (Aldrich, purity 99.99%, Orthorhombic phase) powders were used as raw materials. All powders were dried at 80 °C for 24 h, weighed, and planetary milled in a 250 cm³ volume zirconia jar using a Fritsch Planetary Mill (PULVERISETTE 6), using distilled water as dispersing medium at 2:1 water/powder weight ratio, and 2 mm-diameter yttria-stabilized zirconia balls at 6:1 w/w balls-to-powder ratio. The milling step was set to last 100 min at a rotation speed of 600 rpm. The as-milled slurry was freeze-dried, and the resulting powder sieved and calcined at 700 °C for 9 h. The as-calcined powder was planetary-milled at 400 rpm for 120 min and finally freeze-dried and sieved. Despite the longer procedure, the use of water as the dispersing medium

instead of ethanol allows to obtain softer powders after the freeze drying process, which are both easy to mill and free of stoichiometric or reproducibility issues [8, 9].

2.2 Chemically synthesized KNN powder (KNN_{chem})

A modified Pechini method was used for the synthesis of the KNN powder [15]. Commercially available reactants: potassium acetate (C₂H₃O₂K, 99.0%, Aldrich), sodium acetate (C₂H₃O₂Na, 99.0%, Aldrich), ammonium niobate oxalate tri-hydrate (C₄H₄NNbO₉·3H₂O, 99.99%, Aldrich), citric acid (C₆H₈O₇, 99.5%, Aldrich), acetone (C₃H₆O, 99.9%, Aldrich), and double-distilled water were used as raw materials without further purification. A 1 M solution of citric acid was prepared by dissolving 100 mmol of citric acid in 100 mL of distilled water under stirring. 50 mmol of ammonium niobium oxalate tri-hydrate (ANOT) were then added to the as-prepared citric acid solution, and mixed under reflux and continuous stirring conditions at 60 °C for 30 min. The alkali acetates (25 mmol), with a molar ratio 1:1, were dissolved in 50 ml of water and subsequently added dropwise to the ANOT and citric acid solution previously prepared. The obtained solution was then mixed under reflux and continuous stirring at 60 °C for 30 min. Acetone was then added at room temperature to the clear solution and mixed for 45 min under stirring. The transparent gel was obtained by heating the solution at 100 °C for 3 h. The final gel was further thermally treated in air at 350 °C for 5 h in an alumina crucible. The resulting ashes were ball-milled for 1 h in ethanol (99.9%, Aldrich), dried at 80 °C for 12 h, and calcined at different temperatures (500, 600, 650 and 700 °C) for 5 h in an alumina crucible, and then sieved.

2.3 Sintering

For the preparation of KNN ceramics, 3, 5, 10 and 20% w/w amounts of KNN_{chem} powders were added to the KNN_{SSR} ones. Each KNN_{SSR} + KNN_{chem} powder mixture (KNN_{mix}) was homogenized by ball-milling in ethanol for 1.5 h, dried at 80 °C for 12 h, and then sieved at 250 μm. The so-obtained mixtures were named according to the amounts of KNN_{chem} added to KNN_{SSR}, i.e., as 03KNN_{mix}, 05KNN_{mix}, 10KNN_{mix} and 20KNN_{mix}.

The KNN_{SSR} and KNN_{mix} powders were cold consolidated into discs (Ø = 12 and 20 mm) by die pressing at 200 MPa, followed by cold isostatic pressing at 240 MPa. Finally, the green bodies were sintered in a sealed alumina crucible in the presence of pack powder (KNN with 2 wt% alkali excess, ref. [9]), at 1130 °C for 2 h and 2.5 °C/min heating rate. The sintered discs were then shaped and lapped to a 10:1 diameter-to-thickness ratio. Electrodes were then screen printed onto the samples circular faces using a conductive Ag paste fired at 750 °C for 15 min. The discs were finally poled in silicone oil at 120 °C for 40 min under an applied DC field of 4.5 kV/mm.

2.4 Characterizations

The thermal behaviour of KNN_{chem} precursors and of the corresponding calcined powder at 500 °C was investigated using a simultaneous thermal analyser (STA 449C, Netzsch, Selb, Germany) under air flux, over the 25–1050 °C temperature range at 5 °C/min heating rate. Dilatometric measurements were performed on KNN_{chem} powders uniaxially (200 MPa) and isostatically (240 MPa) pressed into pellets. Dilatometric measurements were performed in air with a 402 CD horizontal dilatometer (Netzsch, Selb, Germany), at 5 K/min heating rate between 20 and 1150 °C.

The crystalline phase of both powders and sintered pellets was analysed by XRD diffractometry (Bruker D8 Advance, Karlsruhe, Germany), using Cu Kα radiation. Patterns were recorded over the 15° ≤ 2θ ≤ 80° range at 2.4°/min scanning rate. For XRD analysis, sintered pellets were ground to a fine powder, which was then sieved and annealed at 700 °C for 30 min to eliminate any lattice strain contributions, and then sieved a second time. Rietveld refinements [43–45] of the diffraction patterns were carried out using GSAS-II© (General Structure Analysis System) software [46]. Hot-stage XRD analysis was also performed in the temperature range between 30 and 800 °C at 10 °C/min to verify the phase evolution of the KNN_{mix} powder during the sintering treatment.

Calculations to determine the K_{0.5}Na_{0.5}NbO₃ phase amount in all spectra were carried out using a structure file (COD DB #2300499 [47]) with noncentrosymmetric A-centred orthorhombic space group (Amm2), while for the K₆Nb_{10.8}O₃₀ phase a structure

file (COD DB #8101301 [48]) with centrosymmetric primitive tetragonal space group was used (P4/mm).

The particle size distributions of the powders were measured using a Malvern Morphologi 4 optical granulometer (Malvern PANalytical, Malvern, UK).

The specific surface area of the KNN powders was measured by the BET method (Sorpty 1750, Carlo Erba).

The green and sintered density values were obtained both by averaging values of the mass-to-geometric volume ratio and by Archimedes' method. The relative density is given as the per cent ratio of the experimental to the theoretical value (4.517 g/cm³).

The morphology and microstructure of the powders and sintered samples were investigated by scanning electron microscopy (SEM-FEG, Carl Zeiss Sigma NTS GmbH, Oberkochen, Germany). For microstructural analysis, sintered samples' polished cross sections were thermally etched at 980 °C for 15 min in air. The grain size distribution of the sintered samples was calculated via image analysis of the SEM micrographs using the ImageJ software (Java, ORACLE, Redwood City, US-CA).

Piezoelectric, dielectric, and mechanical parameters of the samples were determined at least 24 h after poling, by acquiring their room-temperature piezoresonance spectra with an HP 4194A (Hewlett Packard, USA) impedance analyser, detecting resonance and antiresonance frequencies over the 100 Hz–40 MHz range. Room-temperature capacitance and loss tangent were measured at 1 kHz using the same instrument. Dielectric, piezoelectric, and mechanical parameters were calculated according to the 1986 ASTM Standard on Piezoelectricity. The d_{33} piezoelectric coefficient values were separately measured using a Sinocera S 5865 d_{33} -meter calibrated with a 360 pC/N standard sample provided by the manufacturer.

3 Results and discussion

3.1 Optimization of KNN_{chem} calcination

The thermal behaviour of the KNN_{chem} precursor ashes was studied by TG-DSC analysis to optimize their calcination temperature. The thermogravimetric curve (Fig. 1a) shows a first weight loss at 80 °C due to water evaporation, and a larger weight loss (28.1

wt%) at 505 °C, with an onset temperature of 497 °C. This behaviour is related to the combustion reaction of the organic fraction of the gel ashes, and it is confirmed by the sharp exothermic peak registered at the same temperature. Further thermogravimetric events occur at higher temperatures up to about 700 °C, as a consequence of the complete decomposition of the residual carbonaceous species, leading to a total weight loss of 38.6 wt%. After calcining the precursor ashes at 500 °C for 5 h, an experimental weight loss of 33.8 ± 0.4 wt% was registered, confirming an effective combustion of organic compounds.

The XRD patterns in Fig. 1b show that the pure KNN crystal phase is formed already after calcination at 500 °C for 5 h (COD DB #2300499 [47]). Further temperature increase leads to a more crystalline phase in which the splitting of the peaks located at $22^\circ < 2\theta < 24^\circ$ and at $45^\circ < 2\theta < 47^\circ$ becomes detectable, confirming the expected orthorhombic phase at room temperature for calcination temperatures above 600 °C [49–51]. The granulometric curves in Fig. 1c show that the very fine KNN_{chem} particles produced by calcination at 500 °C grow upon calcination at 600 °C and 650 °C, displaying larger particles size than those obtained at 700 °C (see also percentile values displayed in Table 1). The slightly finer mean agglomerate size after calcination at 700 °C can be due to the complete combustion of residual carbonaceous species that occurs at this temperature, as already shown by the TG-DSC analysis (Fig. 1a).

The effect of the calcination temperature on the KNN_{chem} powder's morphology is reported in Fig. 2. The SEM micrographs show that the particles have a cuboidal shape typical of KNN powder [2]; their average size gets larger with increasing calcination temperature, consistently with data shown in Table 1.

Since the aim of this work was that of exploiting the high reactivity of chemically synthesized nano-sized KNN powders when mixed with KNN_{SSR}, those obtained at the lowest temperature (500 °C) were selected. Although this type of powder may still contain unreacted carbonaceous species, their potential higher reactivity in terms of smaller size [42] and their demonstrated ability to fully transform into the orthorhombic phase during the thermal treatments makes this powder a promising candidate material for enhancing the microstructure evolution during the subsequent thermal treatment.

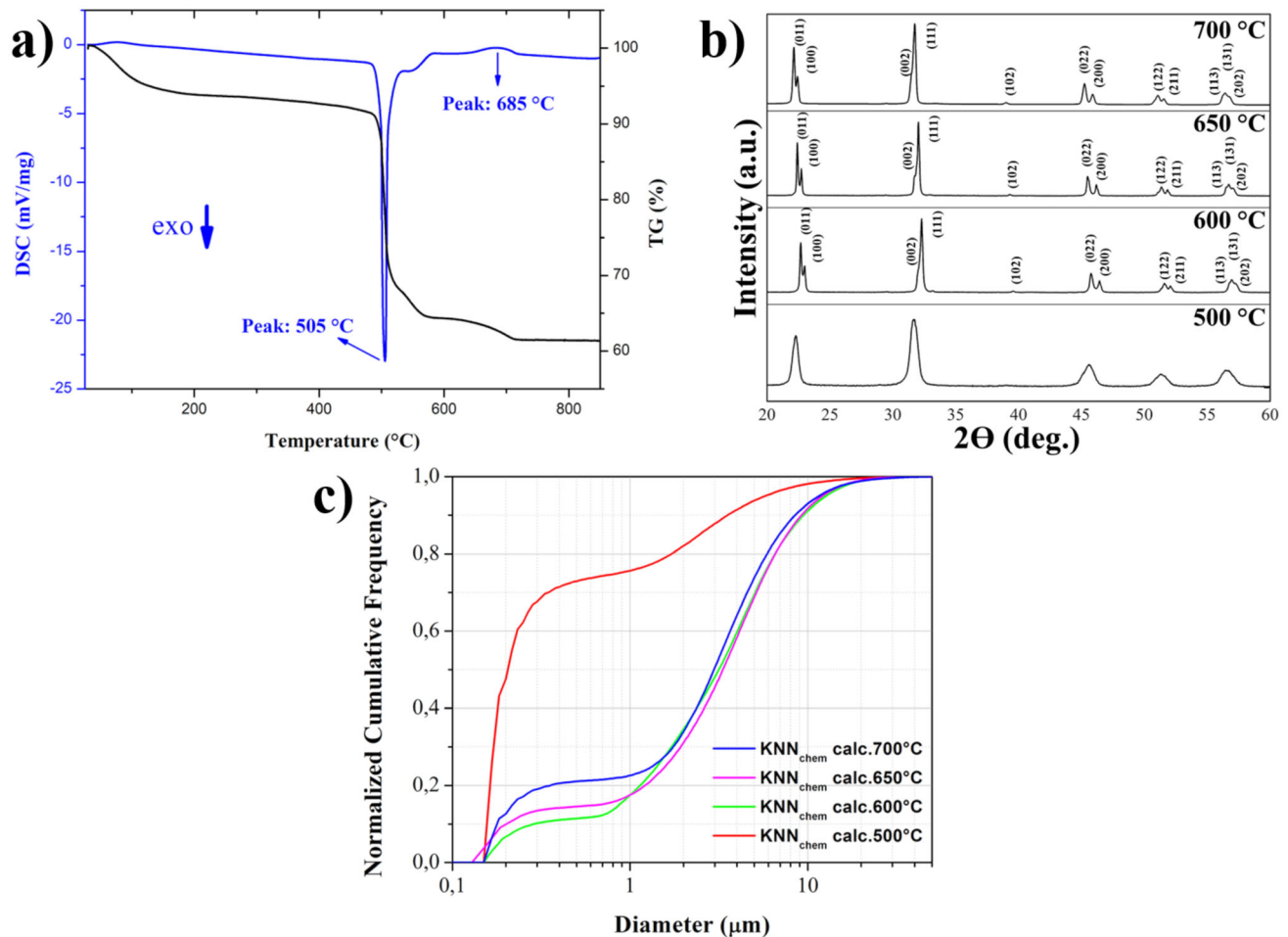


Fig. 1 **a** TG-DSC analysis of precursor ashes of KNN_{chem} . **b** XRD spectra of the KNN_{chem} powders calcined at different temperatures for 5 h, and **c** their corresponding granulometric cumulative curves

Table 1 Effect of different calcination temperatures on KNN_{chem} 's powders particle/agglomerate size distribution and average particle size

Calc. T (°C)	d_{10} (μm , $\varepsilon_a \pm 0.01 \mu\text{m}$)	d_{30}	d_{50}	d_{90}	Average particle size SEM (nm)
500	^a	0.17	0.21	3.54	89 ± 24
600	0.29	1.72	3.17	9.47	365 ± 50
650	0.21	1.93	3.34	9.26	608 ± 65
700	0.18	1.76	2.97	8.50	860 ± 50

d_{10} , d_{20} , d_{50} and d_{90} indicate the 10th, 20th, 50th and 90th percentiles of particles' diameter obtained from their cumulative normalized frequency curves shown in Fig. 1b

^aBelow instrumental detection limit

3.2 Morphological and microstructural characterization of the KNN_{SSR} - KNN_{chem} mixed powders and their sintering behaviour

Granulometric analysis (Fig. 3a) shows that KNN_{SSR} and KNN_{chem} powders have d_{50} values of 0.98 and

0.21 μm , and d_{90} values of 6.82 and 3.54 μm , respectively. Therefore, most of KNN_{chem} particles size is in the nanosized range and thus very fine, as expected with powders obtained via a chemical synthesis route [41]. Moreover, a specific surface area of 21 m^2/g and

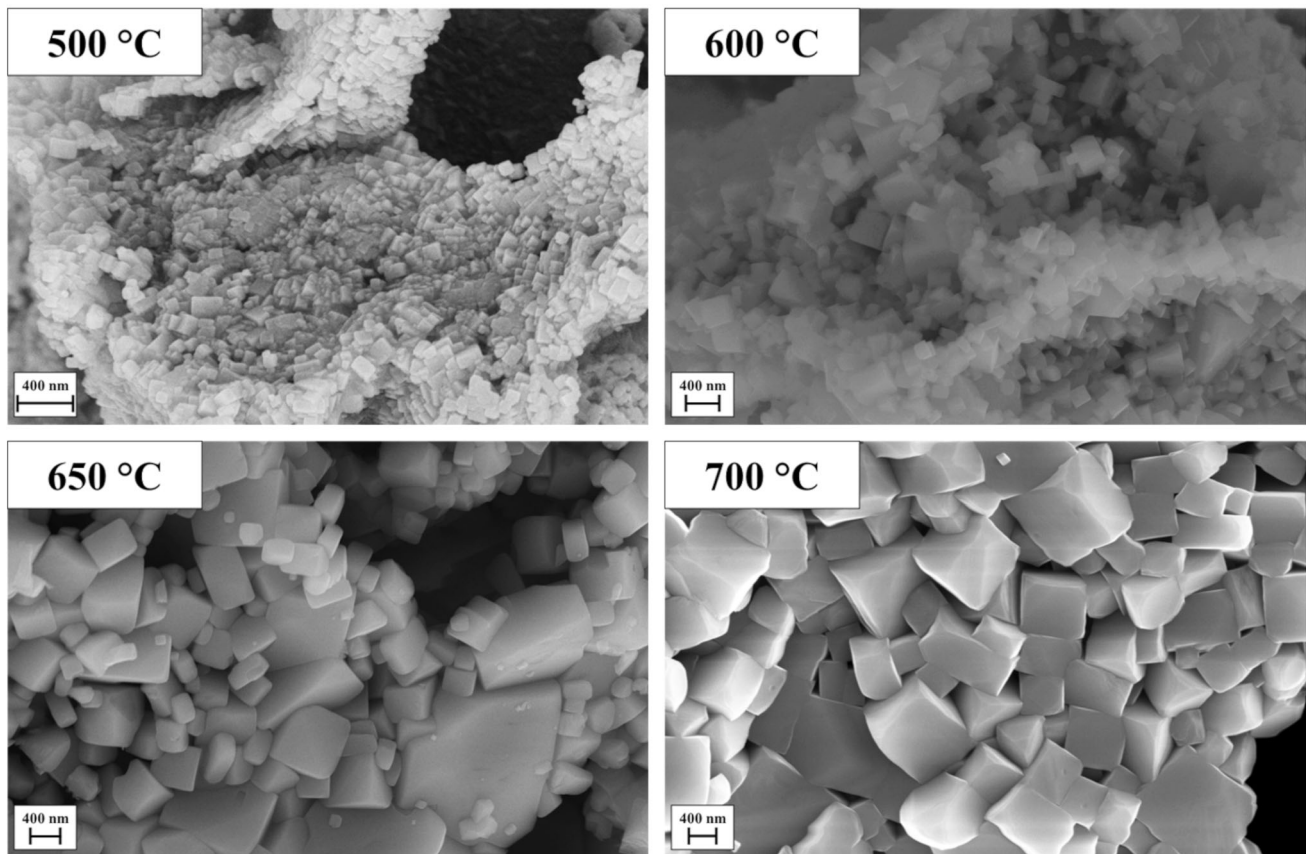


Fig. 2 SEM micrographs of KNN_{chem} powders calcined at different temperatures

$17 \text{ m}^2/\text{g}$ was measured for KNN_{chem} and KNN_{SSR} , respectively.

The SEM micrographs shown in Fig. 3b and c compare the different powder morphologies obtained via the two synthesis routes. Homogeneously sized cuboidal particles with mean particle size in the sub-micrometre range were obtained for the KNN_{chem} powders calcined at $500 \text{ }^\circ\text{C}$, while spheroidal particles with less uniform size were produced by the solid-state reaction. The resulting morphological characteristics confirm the higher potential reactivity of KNN_{chem} powders with respect to the KNN_{SSR} ones.

The XRD spectra of the powders are shown in Fig. 4a. As previously mentioned, KNN_{chem} powders show a pure phase spectrum, without undesired additional phases, in which the peaks match the pattern of the desired stoichiometric perovskite. On the other hand, KNN_{SSR} displays the typical KNN perovskite pattern (COD DB #2300499 [47]), with the presence of an undesired phase indexed as $\text{K}_6\text{Nb}_{10.8}\text{O}_{30}$ (COD DB #8101301 [48]). In addition, the

two reflections peaking at 29.25° and 30.17° may also be attributed to the compound $\text{Na}_2\text{Nb}_4\text{O}_{11}$ (COD DB #7212163 [52]). However, due to the higher amount of $\text{K}_6\text{Nb}_{10.88}\text{O}_{30}$ and the overlapping of the peaks, a precise quantification of the latter is challenging. According to Malic et al. [53], both compounds are in fact formed during the solid-state reaction of the KNN perovskite.

The formation of $\text{K}_6\text{Nb}_{10.88}\text{O}_{30}$ takes place at the interface between the two reactants Nb_2O_5 and K_2CO_3 , while $\text{Na}_2\text{Nb}_4\text{O}_{11}$ formation occurs at the interface between Nb_2O_5 and Na_2CO_3 . When both alkaline species react with Nb_2O_5 , a third species defined as $(\text{K},\text{Na})_2\text{Nb}_4\text{O}_{11}$, isostructural to $\text{Na}_2\text{Nb}_4\text{O}_{11}$, can be formed in which its stoichiometric K/Na ratio may vary over the reaction volume. On a theoretical basis, these three species should gradually disappear while the solid-state reaction evolves towards the formation of the pure stoichiometric perovskite. In this specific case, the presence of these undesired phases can be attributed to a too mild planetary milling treatment [9] during the scaling up

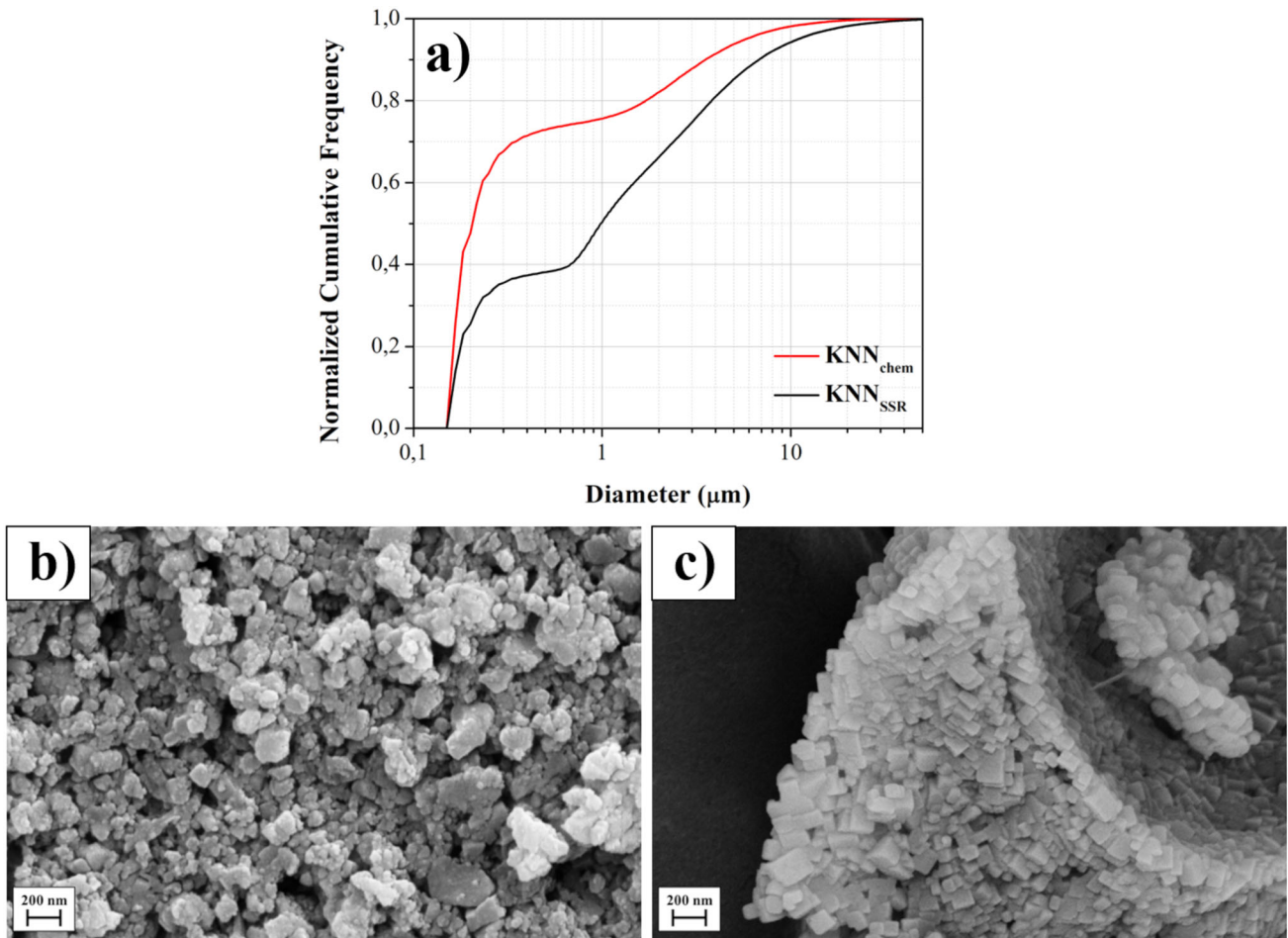


Fig. 3 a Cumulative granulometric curves of KNN_{SSR} and KNN_{chem} . SEM micrographs of **b** KNN_{SSR} and **c** KNN_{chem} calcined at 500 °C for 5 h

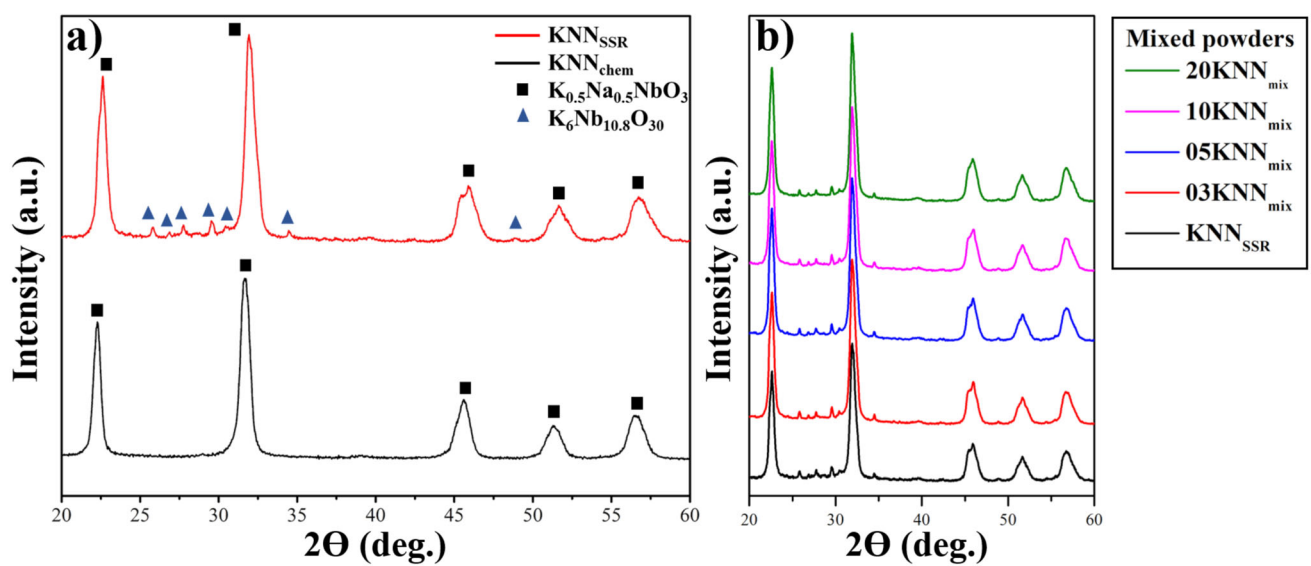


Fig. 4 XRD spectra of KNN_{SSR} and KNN_{chem} powders before (a) and after (b) mixing according to different weight ratios

of the KNN synthesis process. The mechanical energy budget was too low to promote the suitable activation of all reactants and the production of the desired stoichiometric perovskite after the calcination step. In fact, as recently demonstrated by Thong et al. [4], chemical inhomogeneity may arise during solid-state reaction due to less-than-optimal particle size distribution of the precursors and competition among the reactants.

Figure 4b shows the XRD spectra of the powders after mixing (KNN_{mix}) in the 3, 5, 10 and 20 wt% ratios. For all the reported diffractograms, it is possible to recognize a pattern similar to that of unmixed KNN_{SSR} . This demonstrates that the mixing step, performed by a weak ball-milling process, does not lead to a change in crystal structure in which the biggest contribution is ascribed to KNN_{SSR} .

3.3 Crystallographic, microstructural and piezoelectric characterization of the sintered pellets

The density of the *green* bodies and of the sintered samples are summarized in Table 2. In the case of 3 and 5 wt%, the addition of KNN_{chem} does not significantly affect the sintered density while density drops for 10 KNN_{mix} samples. It is also worth noting that the *green* density in the case of KNN_{chem} is about 5% lower than that of KNN_{SSR} . In fact, *green* densities slightly decrease upon addition of KNN_{chem} as a consequence of the different particle size distribution and morphology of the two powders, decreasing the packing ratio.

The XRD spectra of the sintered pellets shown in Fig. 5a) evidence that the undesired $\text{K}_6\text{Nb}_{10.8}\text{O}_{30}$ phase disappears at increasing the KNN_{chem} content, becoming undetectable in the 10 KNN_{mix} and 20 KNN_{mix} samples.

The results of Rietveld refinements performed on the sintered samples are reported in Table 3, while Rietveld refinement plots for KNN_{SSR} and 10 KNN_{mix} are shown in Fig. 5b and c.

Good fitting of the results provides supporting evidence of a negligible difference in the unit cell volumes of the five samples main phase while the presence of the $\text{K}_6\text{Nb}_{10.8}\text{O}_{30}$ phase decreases from 8.5 wt% in KNN_{SSR} to 3.9 wt% in 05 KNN_{mix} . The quantitative phases analysis also confirms that no secondary phase can be detected in the 10 KNN_{mix} and 20 KNN_{mix} samples. In addition, although Rietveld refinements results indicate the presence of KNN stoichiometric phase in all samples, it is worth stressing here that this main phase might feature chemical inhomogeneities, i.e., K/Na stoichiometric ratio different from 50/50 across the whole microstructure. It cannot be excluded, in fact, that such stoichiometric main phase results from statistic overlapping of reflections of phases having a general formula of $\text{K}_x\text{Na}_{1-x}\text{NbO}_3$ but maintaining an overall alkali K/Na ratio of 50/50. Furthermore, as already explained in the previous section, a certain quantity of $\text{Na}_2\text{Nb}_4\text{O}_{11}$ is expected here, though undetected, as a result of the segregation of sodium and potassium during the solid-state reaction.

In order to understand the phase evolution in 10 KNN_{mix} samples, the corresponding powders were analysed by hot-stage XRD measurements over the 25–800 °C temperature range. As reported in Fig. 6a), the intensity of $\text{K}_6\text{Nb}_{10.8}\text{O}_{30}$ reflections (25–30° range) decreases appreciably at temperatures higher than 400 °C, eventually disappearing at 800 °C. The phase evolution in such samples may be explained by taking into consideration the thermal behaviour of pure KNN_{chem} powders. The high reactivity of pure KNN_{chem} samples during the thermal treatment leads to preponderant coarsening processes hindering

Table 2 Effect of KNN_{chem} addition on green and sintered density after sintering at 1130 °C for 2 h

KNN_{chem} content (wt%)	Relative “Green” density (%)	Sintered density (g/cm^3)	Relative sintered density (%)
0 (KNN_{SSR})	65.3	4.16	92.1
3 (03 KNN_{mix})	64.0	4.19	92.7
5 (05 KNN_{mix})	64.4	4.15	91.9
10 (10 KNN_{mix})	64.0	3.87	85.7
20 (20 KNN_{mix})	62.3	4.12	91.2
100 (KNN_{chem})	60.6	–	–

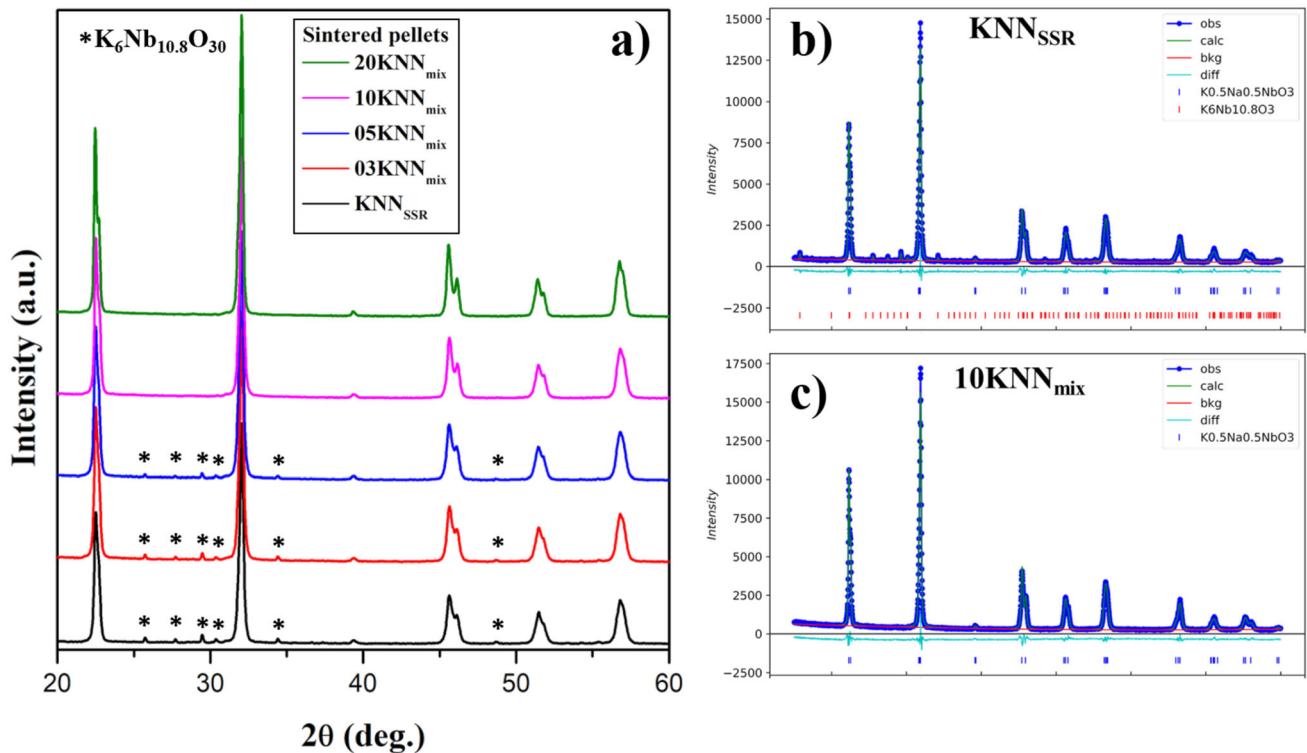


Fig. 5 XRD spectra of the sintered pellets with different KNN_{chem} weight ratios. Rietveld refinement plots of the X-ray powder diffraction patterns collected at RT for **b** KNN_{SSR} and **c** $10\text{KNN}_{\text{mix}}$

Table 3 Refinement agreement factors, quantitative phase analysis, and unit-cell parameters for KNN_{SSR} and KNN_{mix} samples

Sample	Refin. agreement factors			$\text{K}_{0.5}\text{Na}_{0.5}\text{NbO}_3$ (Amm2)					$\text{K}_6\text{Nb}_{10.8}\text{O}_{30}$ (P4/mm)	
	Rw %	χ_r^2	GOF	R_f^2 %	<i>a</i> Å	<i>b</i>	<i>c</i>	Cell volume Å ³	R_f^2 %	Phase fraction wt%
KNN_{SSR}	6.89	2.67	1.63	2.14	3.95	5.64	5.66	126.21	5.29	8.5 ± 0.2
03 KNN_{mix}	6.85	3.04	1.74	2.79	3.96	5.64	5.66	126.25	7.90	4.7 ± 0.8
05 KNN_{mix}	7.04	3.16	1.78	3.92	3.95	5.64	5.66	126.26	6.53	3.9 ± 0.2
10 KNN_{mix}	7.63	3.65	1.91	2.98	3.95	5.64	5.66	126.29	—	—
20 KNN_{mix}	7.61	3.70	1.92	2.88	3.95	5.64	5.66	126.30	—	—

proper densification under the same sintering conditions. It is in fact well known that evaporation/condensation together with surface diffusion, the latter of which is crucial for nanocrystalline powders [54], are material transport mechanisms generally referred as non-densifying mechanisms [2]. In addition, Haugen et al. [22] already reported the difficulty of sintering submicrometric KNN powders. They suggested that small amounts of alkaline hydroxides/carbonates species may form on the surface of particles at room temperature by reacting

with the atmosphere and humidity, resulting in a liquid phase that enhances coarsening and particle growth. On this note, Fig. 6b) shows a pellet consisting of 100 wt% KNN_{chem} powder that was thermally treated at 1130 °C for 2 h. Large crystallites and pores are, in fact, visible on such sample and are likely due to the mentioned coarsening mechanisms. The presence of alkaline carbonates/bicarbonates is confirmed by the thermogravimetric and dilatometric analyses registered onto a 100 wt% KNN_{chem} green pellet. The TG-DSC analysis (Fig. 6c) shows an initial

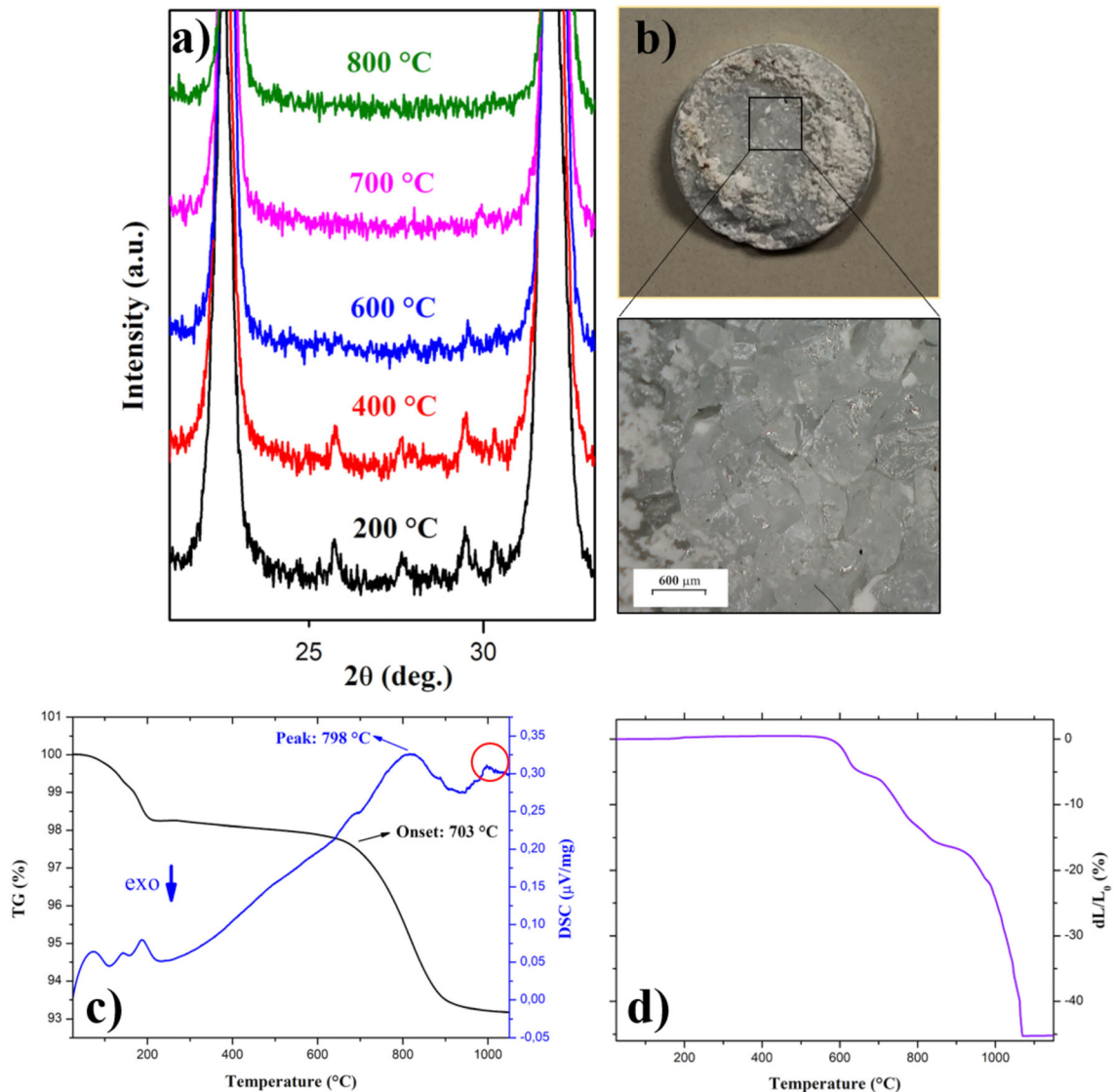


Fig. 6 a Hot-stage XRD spectra and relative temperature of acquisition of $10\text{KNN}_{\text{mix}}$ powders. b Photograph of a KNN_{chem} pellet after thermal treatment at 1130 °C for 2 h and its optical

micrograph of the surface showing large crystals. c TG-DSC and d dilatometric analyses performed on a green pellet of KNN_{chem} calcined at $500\text{ °C} \times 5\text{ h}$

weight loss, along with three endothermic peaks (89 °C , 134 °C and 183 °C) that can likely be attributed to the following reactions: (a) evaporation of adsorbed moisture and dehydration of monohydrates/sesquihydrates carbonates, (b) decomposition of alkaline bicarbonates into carbonates with $\text{H}_2\text{O}/\text{CO}_2$ release, and (c) further dehydration of hydrated carbonates [55–57]. Due to the complex composition of those species on the surface of KNN_{chem} and the associated thermal reaction events that strongly depend on environmental moisture and local CO_2 concentration, it is impossible to assign such peaks with greater accuracy. A subsequent weight loss

occurs in the $750\text{--}900\text{ °C}$ range with a correlated endothermic peak, which is likely compatible with a decarbonation reaction of alkaline carbonates, which furthermore confirms the presence of the species on the surface of KNN_{chem} particles [58, 59]. On the other hand, alkaline hydroxides could not be detected by TG-DSC, even though their presence is expected, since such compounds are involved in the formation of bicarbonates/carbonates by reacting with moisture and CO_2 . In addition, since the phase evolution of KNN_{SSR} has been verified to be re-activated from 400 °C on, this temperature matches the

melting points of potassium (360 °C) and sodium hydroxides (318 °C) [55–59].

Figure 6d shows KNN_{chem} 's dilatometric curve. A multi-step shrinkage pattern starts at the onset temperature of ca. 595 °C. A second shrinkage occurs between 650 and 850 °C. Finally, the dilatometric curve shows the onset of sintering at 935 °C, with a total shrinkage of 45% at about 1060 °C. However, the curve does not reach a plateau due to an instrumental signal loss caused by incipient melting of the sample, as confirmed by the endothermic peak at about 1000 °C in the DSC curve (Fig. 6c, red circle).

A possible explanation of the KNN_{chem} contribution on the phase evolution mechanism of KNN_{mix} samples is sketched in Fig. 7.

As previously described, KNN_{SSR} powders are characterized by particles containing several phases while maintaining an overall stoichiometric 50/50 ratio of the two alkaline elements. Potassium and sodium have different diffusion rates, determining a segregation of each alkaline element in the microstructure, especially in the present case, in which optimal grain size distribution of each reactant

is not reached after milling. Thus, the formation of the expected stoichiometric $\text{K}_{0.5}\text{Na}_{0.5}\text{NbO}_3$ perovskite is accompanied by the formation of $\text{K}_6\text{Nb}_{10.8}\text{O}_{30}$ that may result from a preferential reaction between K_2CO_3 and Nb_2O_5 . Subsequently, formation of $\text{Na}_2\text{Nb}_4\text{O}_{11}$ and $\text{K}_x\text{Na}_{1-x}\text{NbO}_3$ potassium-deficient phases is expected, but their presence is difficult to detect in this case. The highly reactive KNN_{chem} powders added to KNN_{SSR} generate a transient liquid phase at 400 °C, originating from alkaline carbonates and hydroxides at the surface of KNN_{chem} grains, which enhances the diffusion of alkaline species across the microstructure. Potassium and sodium species diffuse towards and inside every surrounding grain, resulting in reactions among the non-stoichiometric phases and the free-species generated in situ by KNN_{chem} .

The overall result of such event is the compensation of the stoichiometry and further conversion of the undesired phase to stoichiometric perovskite. This phase conversion occurs at temperatures ranging between 400 and 800 °C, thus over a lower and wider temperature range than that of frequently

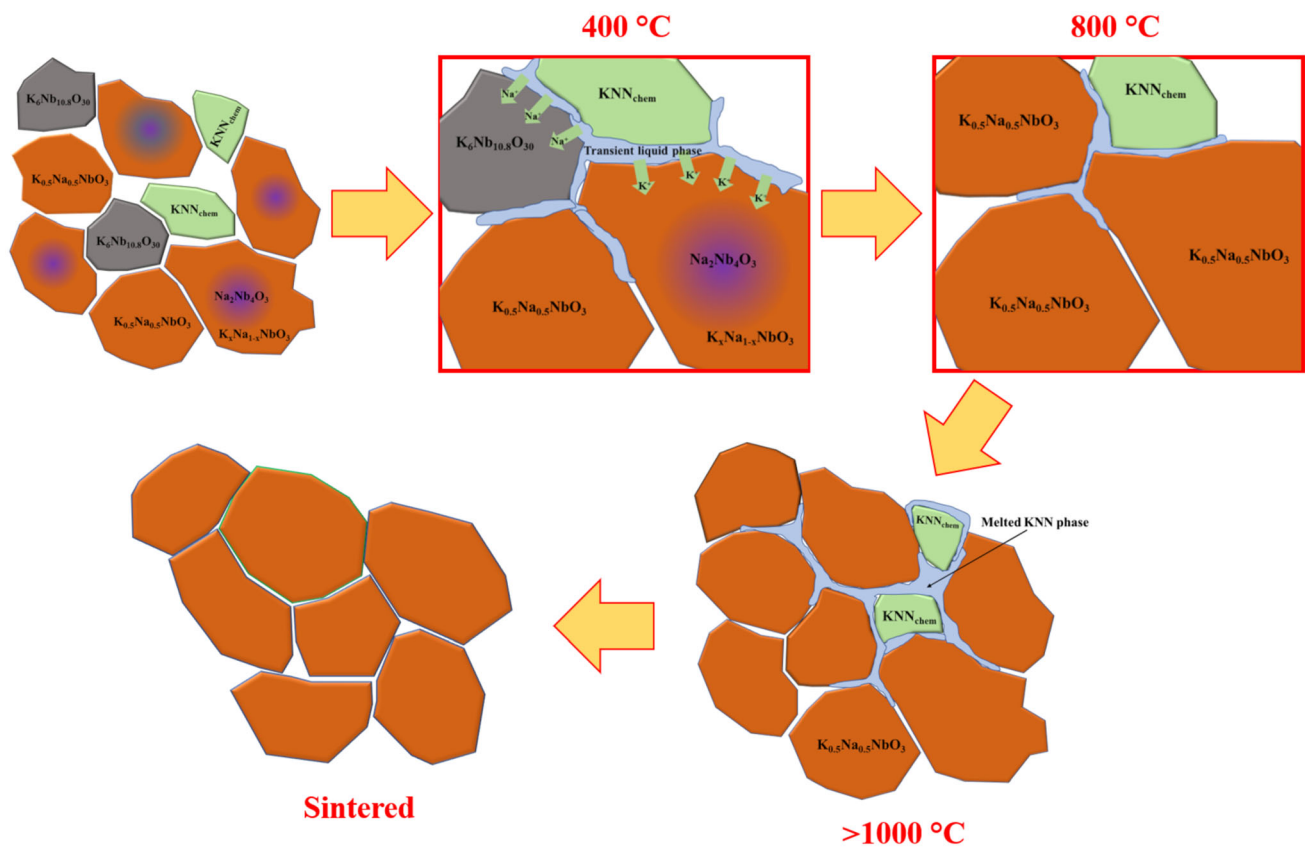


Fig. 7 Depiction of the hypothesized mechanism of KNN_{chem} powder's contribution on phase evolution in KNN_{mix} samples

reported calcination temperatures for KNN [2], in which the perovskite phase is expected to form by solid-state reaction processes. It can be assessed that KNN_{chem} powder's role is the re-activation of the solid-state reaction leading to the formation of the stoichiometric perovskite. KNN_{chem} 's grains are not fully consumed as the reaction goes on and contribute to the grain growth process as well as the evolution of the microstructure during sintering. Grains consisting of stoichiometric phase are thought to interact with the KNN_{chem} liquid phase as well, but such interaction only results in grain growth and changes in grain shape and morphology, leaving the same starting stoichiometry unaffected.

In case of less than 10 wt % addition of KNN_{chem} , the amount of the same is not sufficient to promote full phase conversion. Similarly, without addition of KNN_{chem} , phase conversion is not re-activated in the KNN_{SSR} powder.

SEM micrographs of the thermally etched cross sections are shown in Fig. 8. Microstructural analysis highlights that even though the grain size is mostly in the sub-micrometric range, featuring few large grains surrounded by a large number of smaller ones, no substantial microstructural difference is detectable for the KNN_{SSR} , 03 KNN_{mix} and 05 KNN_{mix} samples. Small globular-shaped grains are present in the KNN_{SSR} and 03 KNN_{mix} samples (red circles in Fig. 8), which can likely be attributed to the $\text{K}_6\text{Nb}_{10.8}\text{O}_{30}$ phase. These grains become smaller and more uniformly distributed with increasing KNN_{chem} content. In addition, density values measured after sintering at 1130 °C (Table 2) are comparable, suggesting that small amounts of KNN_{chem} powder (3 and 5 wt%) do not significantly affect the densification and sintering behaviour of KNN_{SSR} .

In the case of the 10 KNN_{mix} sample, it is possible to notice the formation of a residual micro-porosity, evenly distributed across the section. This agrees with the low sintered density value reported in Table 2 and could be explained by the larger amount of KNN_{chem} . The use of two KNN powders with different surface reactivity and morphological characteristics may lead to heterogeneous shrinkage [60] and, therefore, lower density values due to different densification and shrinkage mechanisms. On the other hand, the use of 20 wt% of KNN_{chem} powder exacerbates this phenomenon, leading to a heterogeneous microstructure consisting of well-densified regions alternating with highly porous ones, with an

overall density value slightly higher than the 10 KNN_{mix} sample. Such microstructural inhomogeneity may be the result of preferential segregation of KNN_{chem} and KNN_{SSR} powders in the starting green body. Furthermore, rounded-edges grains can be observed in well-densified regions of 20 KNN_{mix} microstructure that may result from a liquid-phase sintering process, thus confirming the hypothesized mechanism. In the case of less densified regions, such mechanism may have hindered proper densification. These results are also confirmed by the cumulative normalized frequencies of grain size of the sintered samples plotted in Fig. 8. The average grain size initially decreases from 0.40 μm in KNN_{SSR} to 0.33 μm and 0.35 μm in 05 KNN_{mix} and 10 KNN_{mix} , respectively, then increases to 0.65 μm in 20 KNN_{mix} . Moreover, the presence of larger amounts of KNN_{chem} powder not only changes the average grain size, but also its distribution. For example, in KNN_{SSR} , the grain size is mostly distributed within the 0.15–0.42 μm range. Increasing the KNN_{chem} content results in an increase in the population of smaller grains around the mean value. In 10 KNN_{mix} , the grain size is evenly distributed over the 0.10–0.46 μm range with a very small number of larger grains. However, the highest KNN_{chem} content leads to a segregation of KNN_{SSR} and KNN_{chem} in different areas of the green body and, as a consequence, of the sintered ceramic, leading to inhomogeneous regions with larger average grain size due to the coarsening of KNN_{chem} nanopowders promoted by the surface diffusion mechanism.

These results suggest that the use of a too high amount of KNN_{chem} powder negatively affects the final KNN ceramic microstructure, even though KNN_{chem} promotes a chemical homogenization and yields a pure stoichiometric KNN perovskite.

The piezoelectric and dielectric characterization (Table 4) highlights that the addition of chemically synthesized KNN_{chem} has considerable effect on the piezoelectric and dielectric properties of the sintered samples. The main noticeable effect is the increased d_{33} coefficient, which progressively increases from 76 pC/N at 0 wt% KNN_{chem} to 115 pC/N at 10 wt% KNN_{chem} . Such d_{33} value is comparable to the highest d_{33} values reported in the literature for conventional processing and sintering of undoped stoichiometric KNN [39]. d_{33} values between 65 and 117 pC/N were in fact reported for pure KNN system [8, 61–64] synthesized starting from planetary milled

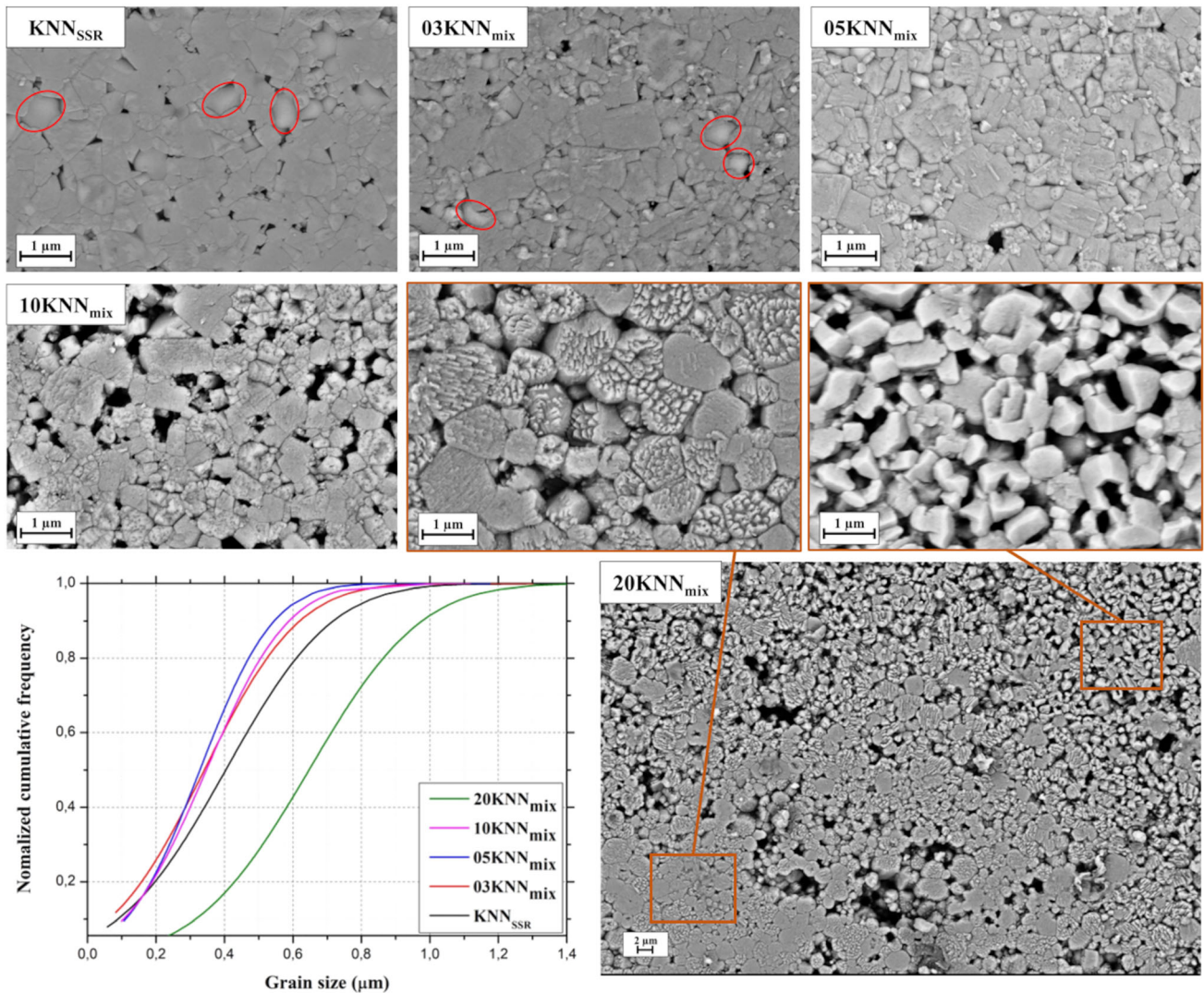


Fig. 8 SEM micrographs of polished and thermally etched cross-sectional surfaces of sintered KNN samples. On the left bottom side, plot of normalized grain size cumulative frequency curves

Table 4 Piezoelectric and dielectric properties of sintered pellets

Sample	Relative Sint. density %	d_{33} pC/N	k_t	k_p	$\tan(\delta)$ 10^{-3}	ϵ_{33}^T
KNN _{SSR}	92.1	76	0.37	0.25	151	658
03KNN _{mix}	92.7	95	0.38	0.27	123	573
05KNN _{mix}	91.9	113	0.44	0.31	60	492
10KNN _{mix}	85.7	115	0.48	0.28	566	801
20KNN _{mix}	91.2	9	0.26	0.13	732	1908

precursors and finally sintered in air at temperatures ranging between 1100 and 1140 °C. It is worth noting that d_{33} values seem to be independent on density, which is an interesting peculiarity of the materials studied in the present work.

The same trend was observed for the electromechanical thickness and planar coupling factor k_t and k_p , respectively. The increase in d_{33} and k values seems to be concurrent with the progressive disappearance of the secondary phase with increasing content of KNN_{chem}, as previously demonstrated by

the Rietveld's refinements studies. Nonetheless, the drop of d_{33} and k values in 20KNN_{mix} samples must be attributed to their inhomogeneous microstructure, even though these samples present pure KNN stoichiometric phase.

The trend of the dielectric parameters ϵ_{33}^T and $\tan(\delta)$ is similar, characterized by slightly lower values up to 5 wt% of KNN_{chem} content, followed by an increase in both ϵ_{33}^T and $\tan(\delta)$ values that can be explained with augmented porosity in sintered samples containing more than 10 wt% KNN_{chem}. Other dielectric measurements at different frequencies are reported in Figure S1 of the Supplementary Information. With the only exception of sample 10KNN_{mix}, dielectric constant's magnitude values fall into the $100 \leq \epsilon_R \leq 2000$ range for $1 \text{ kHz} \leq f \leq 1 \text{ MHz}$, in reasonable agreement with room-temperature values given in the literature. Dielectric loss tangent values generally indicate poor dielectric performance of all samples over said range, with the possible exception of sample 5KNN_{mix} whose loss tangent has values close to zero. Sample 10KNN_{mix}'s dielectric performance is very poor, with a value of the dielectric loss tangent about 2.7 at 100 Hz. The influence of the addition of KNN_{chem} on P–E loops of the corresponding ceramics was also investigated (Figure S2). The shown P–E loops are standard ferroelectric hysteresis loops, featuring polarization values about $15 \mu\text{C}/\text{cm}^2$ at 30 kV/cm electric field, with remnant polarization of 3.25 and $3.44 \mu\text{C}/\text{cm}^2$, for KNN_{SSR} and 5KNN_{mix}, respectively, and coercive field values about 4.5 kV/cm. Similar values have been presented in the literature.

As previously explained, the main reason for the poor piezoelectric performance of KNN_{SSR} is mainly attributed to insufficiently energetic milling treatment and thus to the presence of a secondary detrimental phase in addition to the pure KNN perovskite one.

According to piezoelectric and dielectric measurements, an increase in piezoelectric properties can be observed with increasing content of KNN_{chem}. Samples 05KNN_{mix} and 10KNN_{mix} should be considered as the best performing piezoceramics in this work. However, 10KNN_{mix} shows high $\tan(\delta)$ and poor sintered density values, in spite of being constituted of pure KNN perovskite phase, with uniform and well-distributed grains. On the other hand, 05KNN_{mix} shows improved d_{33} and k_t values along

with acceptable density value and grain size distribution whose average value is not so different to that of KNN_{SSR}. The presence of the small amount of undesired phase (about 3.9 wt%) in 05KNN_{mix} seems to slightly affect the piezoelectric performance with respect to 10KNN_{mix}.

Therefore, a balanced addition of KNN_{chem} can reduce the content of the undesired phase, resulting in better piezoelectric performances. The further addition of KNN_{chem} up to 10 wt% can effectively yield better piezoelectric response as well as decreased densities.

The addition of 20 wt% of KNN_{chem} was demonstrated to be beneficial for stoichiometry homogenization (phase purity), but it is detrimental for the microstructure (increased average grain size and heterogeneity), and therefore for the piezoelectric response.

Results as a whole suggest that the best KNN piezoelectric performance can be obtained with the right combination of all these parameters (purity of crystallographic phase, average grain size and grain size distribution, density, characteristics of the starting powders etc.) and that it can be improved by the addition of chemically synthesized pure-phase KNN powders combining right stoichiometry and high reactivity.

4 Conclusions

This work investigates the possibility of exploiting the high reactivity of a chemically synthesized KNN powder, to provide a simple, effective, and easily scalable strategy to eliminate secondary phases and improve the final piezoelectric performance without using complex, expensive, and unconventional production technologies.

Two powders with stoichiometric formula $\text{K}_{0.5}\text{Na}_{0.5}\text{NbO}_3$ were produced through two different methods: mechanochemically activated solid-state synthesis (KNN_{SSR}) and chemical synthesis (KNN_{chem}). 500 °C for 5 h has been selected as optimal calcination condition to obtain fine and highly reactive KNN_{chem} powders. KNN_{SSR} powders were mixed with KNN_{chem} according to different weight percentages (3, 5, 10 and 20%) and then sintered. The highly reactive KNN_{chem} particles play an active role in reducing the amount of undesired crystal phases, further converting them into orthorhombic

stoichiometric KNN perovskite. A possible mechanism has been proposed to explain such chemical homogenization: alkaline hydroxides/carbonates/bicarbonates formed on the surface of highly reactive KNN_{chem} particles promote a liquid-phase formation at temperature higher than 400 °C. The liquid phase enhances the diffusion of alkaline species across the whole microstructure, leading to a re-activation of perovskite formation. During sintering, the residual highly reactive fine powders contribute to grain growth and interdiffusion. Piezoelectric constants d_{33} and k_t improve with increasing KNN_{chem} content up to 10 wt%, and then decrease in 20 KNN_{mix} sample. In particular, the d_{33} piezoelectric charge constant increases from 76 to 115 pC/N at 10 wt% of KNN_{chem} fraction. Sintered density values do not increase with further addition of KNN_{chem} ; therefore, 05 KNN_{mix} samples are considered the best compromise between piezoelectric ($d_{33} = 113$ pC/N, $k_t = 0.44$) and dielectric properties ($\epsilon_{33}^T = 492$, $\tan(\delta) = 60 \times 10^{-3}$) and sintered density (91.9%), even though an amount of 3.9 wt% of undesired phase is still present. The presence of such undesired phase is not beneficial for the piezoelectric performance, but it is demonstrated here that its content can be decreased with the addition of KNN_{chem} , thus enhancing the piezoelectric properties.

The results of this work confirm that it is possible to improve the stoichiometric homogenization and piezoelectric properties of KNN sintered pellets obtained from poorly activated starting powders by adding chemically synthesized KNN powders with the same stoichiometry. This approach could be successfully applied to more complex compositions to promote the industrial scale production of reliable and performing lead-free ceramics by conventional synthesis and sintering routes.

Acknowledgements

This research was carried out in the framework of the Joint Research Laboratory between Politecnico di Milano and STMicroelectronics with the aim at developing innovative MEMS devices and technological processes. Authors would like to acknowledge the “Functional Sintered Materials (Funtasma)” Interdepartmental Laboratory of Politecnico di Milano, where this research activity was partially developed. Support by the Italian Ministry for

Education, University and Research through the project Department of Excellence LIS4.0 (Integrated Laboratory for Lightweight e Smart Structures) is also acknowledged. EM acknowledges the support from the project DIGIMAN funded by POR FESR 2014-2020. AZIONE 1.2.2. Regione Emilia Romagna. Authors would also like to thank Mr. Claudio Capiani (ISTEC-CNR) for his valuable technical assistance and Dr. Sonia Conte (ISTEC-CNR) for fruitful discussion on XRD analysis and related refinements.

Author contributions

EM contributed to writing—original draft, methodology, and investigation. EM contributed to investigation, validation, conceptualization, and writing—review and editing. RB contributed to methodology and investigation. MM contributed to methodology investigation, and review and editing. CB contributed to investigation, validation, and writing—review and editing. CG contributed to writing—review and editing and supervision. NL contributed to conceptualization, supervision, and project administration.

Funding

The authors declare that no funds, grants, or other support were received during the preparation of this manuscript.

Data availability

All data generated or analysed during this study are included in this published article.

Declarations

Competing interests The authors have no competing interests to declare that are relevant to the content of this article.

Supplementary Information: The online version contains supplementary material available at <http://doi.org/10.1007/s10854-022-08854-x>.

Open Access This article is licensed under a Creative Commons Attribution 4.0 International License, which permits use, sharing, adaptation, distribution

and reproduction in any medium or format, as long as you give appropriate credit to the original author(s) and the source, provide a link to the Creative Commons licence, and indicate if changes were made. The images or other third party material in this article are included in the article's Creative Commons licence, unless indicated otherwise in a credit line to the material. If material is not included in the article's Creative Commons licence and your intended use is not permitted by statutory regulation or exceeds the permitted use, you will need to obtain permission directly from the copyright holder. To view a copy of this licence, visit <http://creativecommons.org/licenses/by/4.0/>.

References

- H.C. Thong, C. Zhao, Z. Zhou, C.F. Wu, Y.X. Liu, Z.Z. Du, J.F. Li, W. Gong, K. Wang, *Mater. Today* **29**, 37–48 (2019). <https://doi.org/10.1016/j.mattod.2019.04.016>
- B. Malič, J. Koruza, J. Hreščak, J. Bernard, K. Wang, J.G. Fisher, A. Benčan, *Materials* **8**, 8117–8146 (2015). <https://doi.org/10.3390/ma8125449>
- A. Popović, L. Bencze, J. Koruza, B. Malič, *RSC Adv.* **5**, 76249–76256 (2015). <https://doi.org/10.1039/C5RA11874C>
- H.-C. Thong, A. Payne, J.-W. Li, Y.-Y.-S. Cheng, J.L. Jones, K. Wang, *Acta Mater.* **211**, 116833 (2021). <https://doi.org/10.1016/j.actamat.2021.116833>
- J. Hreščak, A. Bencan, T. Rojac, B. Malič, *J. Eur. Ceram. Soc.* **33**, 3065–3075 (2013). <https://doi.org/10.1016/j.jeurceramso.2013.07.006>
- Y. Zhen, J.F. Li, *J. Am. Ceram. Soc.* **90**, 3496–3502 (2007). <https://doi.org/10.1111/j.1551-2916.2007.01977.x>
- H.C. Thong, Z. Xu, C. Zhao, L.Y. Lou, S. Chen, S.Q. Zuo, J.F. Li, K. Wang, *J. Am. Ceram. Soc.* **102**, 836–844 (2019). <https://doi.org/10.1111/jace.16070>
- B. Chen, P. Liang, D. Wu, X. Zhao, X. Qiao, Z. Peng, L. Wei, X. Chao, Z. Yang, *Powder Technol.* **346**, 248–255 (2019). <https://doi.org/10.1016/j.powtec.2019.01.039>
- R. Beltrami, E. Mercadelli, C. Baldisserrri, C. Galassi, F. Braghin, N. Lecis, *Powder Technol.* **375**, 101–108 (2020). <https://doi.org/10.1016/j.powtec.2020.07.098>
- J.F. Li, K. Wang, F.Y. Zhu, L.Q. Cheng, F.Z. Yao, *J. Am. Ceram. Soc.* **96**, 3677–3696 (2013). <https://doi.org/10.1111/jace.12715>
- J. Xing, T. Zheng, J. Wu, D. Xiao, J. Zhu, *J. Adv. Dielectr.* **8**, 1830003 (2018). <https://doi.org/10.1142/S2010135X18300037>
- X. Lv, J. Zhu, D. Xiao, X.X. Zhang, J. Wu, *Chem. Soc. Rev.* **49**, 671–707 (2020). <https://doi.org/10.1039/C9CS00432G>
- K. Chen, J. Ma, C. Shi, W. Wu, B. Wu, *J. Alloys Compd.* **852**, 156865 (2021). <https://doi.org/10.1016/j.jallcom.2020.156865>
- T. Zheng, J. Wu, D. Xiao, J. Zhu, *Scripta Mater.* **94**, 25–27 (2015). <https://doi.org/10.1016/j.scriptamat.2014.09.008>
- N. Senes, A. Iacomini, N. Domingo, S. Enzo, G. Mulas, S. Cuesta-Lopez, S. Garroni, *Phys. Status Solidi (A)* **215**, 1700921 (2018). <https://doi.org/10.1002/pssa.201700921>
- K.I. Kakimoto, Y. Hayakawa, I. Kagomiya, *J. Am. Ceram. Soc.* **93**, 2423–2426 (2010). <https://doi.org/10.1111/j.1551-2916.2010.03748.x>
- S. Kumar, M. Shandilya, S. Thakur, N. Thakur, G.A. Kaur, *J. Sol-Gel Sci. Technol.* **92**, 215–223 (2019). <https://doi.org/10.1007/s10971-019-05077-1>
- L.A. Ramajo, F. Rubio-Marcos, A. Del Campo, J.F. Fernández, M.S. Castro, R. Parra, *Ceram. Int.* **40**, 14701–14712 (2014). <https://doi.org/10.1016/j.ceramint.2014.06.059>
- Y. Zhao, R. Huang, R. Liu, H. Zhou, W. Zhao, *Curr. Appl. Phys.* **13**, 2082–2086 (2013). <https://doi.org/10.1016/j.cap.2013.08.015>
- N. Liu, K. Wang, J.F. Li, Z. Liu, *J. Am. Ceram. Soc.* **92**, 1884–1887 (2009). <https://doi.org/10.1111/j.1551-2916.2009.03126.x>
- R. López, F. González, M.P. Cruz, M.E. Villafuerte-Castrejon, *Mater. Res. Bull.* **46**, 70–74 (2011). <https://doi.org/10.1016/j.materresbull.2010.09.034>
- A.B. Haugen, F. Madaro, L.P. Björkeng, T. Grande, M.A. Einarsrud, *J. Eur. Ceram. Soc.* **35**, 1449–1457 (2015). <https://doi.org/10.1016/j.jeurceramsoc.2014.11.011>
- Y. Chang, S.F. Poterala, Z. Yang, S. Trolier-McKinstry, G.L. Messing, *J. Mater. Res.* **25**, 687–694 (2010). <https://doi.org/10.1557/JMR.2010.0084>
- Y. Li, C. Hui, M. Wu, Y. Li, Y. Wang, *Ceram. Int.* **38**, S283–S286 (2012). <https://doi.org/10.1016/j.ceramint.2011.04.102>
- A.B. Haugen, G.H. Olsen, F. Madaro, M.I. Morozov, G. Tutuncu, J.L. Jones, T. Grande, M.A. Einarsrud, *J. Am. Ceram. Soc.* **97**, 3818–3825 (2014). <https://doi.org/10.1111/jace.13223>
- L. Li, W. Bai, Y. Zhang, B. Shen, J. Zhai, *J. Alloys Compd.* **622**, 137–142 (2015). <https://doi.org/10.1016/j.jallcom.2014.10.014>
- B.P. Zhang, J.F. Li, K. Wang, H. Zhang, *J. Am. Ceram. Soc.* **89**, 1605–1609 (2006). <https://doi.org/10.1111/j.1551-2916.2006.00960.x>
- J.F. Li, K. Wang, B.P. Zhang, L.M. Zhang, *J. Am. Ceram. Soc.* **89**, 706–709 (2006). <https://doi.org/10.1111/j.1551-2916.2005.00743.x>
- M. Bah, F. Giovannelli, F. Schoenstein, G. Feuillard, E. Le Clezio, I. Monot-Laffez, *Ceram. Int.* **40**, 7473–7480 (2014). <https://doi.org/10.1016/j.ceramint.2013.12.097>

30. T. Morshed, E.U. Haq, C. Silien, S.A.M. Tofail, M.A. Zubair, M.F. Islam, *IEEE Trans. Dielectr. Insul.* **27**, 1428–1432 (2020). <https://doi.org/10.1109/TDEI.2020.008820>
31. R.E. Jaeger, L. Egerton, *J. Am. Ceram. Soc.* **45**, 209–213 (1962). <https://doi.org/10.1111/j.1151-2916.1962.tb11127.x>
32. Z. Yu, X. Chen, Y. Su, H. Lian, J. Lu, J. Zhou, P. Liu, *J. Mater. Sci.* **54**, 13457–13466 (2019). <https://doi.org/10.1007/s10853-019-03850-9>
33. Z. Li, H. Sun, X. Liu, H. Sui, H. Guo, *Ceram. Int.* **46**, 11617–11621 (2020). <https://doi.org/10.1016/j.ceramint.2020.01.191>
34. M. Feizpour, H.B. Bafrooei, R. Hayati, T. Ebadzadeh, *Ceram. Int.* **40**, 871–877 (2014). <https://doi.org/10.1016/j.ceramint.2013.06.081>
35. H.S. Devi, M. Maisnam, *Integr. Ferroelectr.* **202**, 204–209 (2019). <https://doi.org/10.1080/10584587.2019.1674838>
36. J. Bernard, A. Benčan, T. Rojac, J. Holc, B. Malič, M. Kosec, *J. Am. Ceram. Soc.* **91**, 2409–2411 (2008). <https://doi.org/10.1111/j.1551-2916.2008.02447.x>
37. K. Chen, F. Zhang, J. Zhou, X. Zhang, C. Li, L. An, *Ceram. Int.* **41**, 10232–10236 (2015). <https://doi.org/10.1016/j.ceramint.2015.04.131>
38. N.M. Hagh, B. Jadidian, A. Safari, *J. Electroceram.* **18**, 339–346 (2007). <https://doi.org/10.1007/s10832-007-9171-x>
39. H.C. Thong, C. Zhao, Z.X. Zhu, X. Chen, J.F. Li, K. Wang, *Acta Mater.* **166**, 551–559 (2019). <https://doi.org/10.1016/j.actamat.2019.01.012>
40. H. Du, Z. Li, F. Tang, S. Qu, Z. Pei, W. Zhou, *Mater. Sci. Eng. B* **131**, 83–87 (2006). <https://doi.org/10.1016/j.mseb.2006.03.039>
41. T. Ring, *Fundamentals of Ceramic Powder Processing and Synthesis*, 1st edn. (Academic Press Inc., San Diego, 1996)
42. W.D. Kingery, H.K. Bowen, D.R. Uhlmann, *Introduction to Ceramics*, 1st edn. (Wiley, New York, 1976)
43. H.M. Rietveld, *Acta Crystallogr.* **22**, 151–152 (1967). <https://doi.org/10.1107/S0365110X67000234>
44. G. Malmros, J.O. Thomas, *J. Appl. Crystallogr.* **10**, 7–11 (1977). <https://doi.org/10.1107/S0021889877012680>
45. L.B. McCusker, R.B. Von Dreele, D.E. Cox, D. Louër, P. Scardi, *J. Appl. Crystallogr.* **32**, 36–50 (1999). <https://doi.org/10.1107/S0021889898009856>
46. B.H. Toby, R.B. Von Dreele, *J. Appl. Crystallogr.* **46**, 544–549 (2013). <https://doi.org/10.1107/S0021889813003531>
47. B. Orayech, A. Faik, G.A. López, O. Fabelo, J.M. Igartua, *J. Appl. Crystallogr.* **48**, 318–333 (2015). <https://doi.org/10.1107/S1600576715000941>
48. P. Becker, P. Held, *Z. Kristallogr. NCS* **215**, 319–320 (2000). <https://doi.org/10.1515/ncrs-2000-0306>
49. D.W. Baker, P.A. Thomas, N. Zhang, A.M. Glazer, *Appl. Phys. Lett.* **95**, 091903 (2009). <https://doi.org/10.1063/1.3212861>
50. J. Tellier, B. Malič, B. Dkhil, D. Jenko, J. Cilensek, M. Kosec, *Solid State Sci.* **11**, 320–324 (2009). <https://doi.org/10.1016/j.solidstatesciences.2008.07.011>
51. P. Kumar, M. Pattanaik, *Ceram. Int.* **39**, 65–69 (2013). <https://doi.org/10.1016/j.ceramint.2012.05.093>
52. N. Masó, A.R. Westa, *J. Mater. Chem.* **20**, 2082–2084 (2010). <https://doi.org/10.1039/B921115B>
53. B. Malic, D. Jenko, J. Holc, M. Hrovat, M. Kosec, *J. Am. Ceram. Soc.* **91**, 1916–1922 (2008). <https://doi.org/10.1111/j.1551-2916.2008.02376.x>
54. R. Chaim, M. Levin, A. Shlayer, C. Estournès, *Adv. Appl. Ceram.* **107**, 159–169 (2008). <https://doi.org/10.1179/174367508X297812>
55. M. Hartman, O. Trnka, V. Vesely, K. Svoboda, *Chem. Eng. Commun.* **185**, 1–16 (2001). <https://doi.org/10.1080/00986440108912851>
56. Y. Duan, D.R. Luebke, H.W. Pennline, B. Li, M.J. Janik, J. Woods Halley, *J. Phys. Chem. C* **116**, 14461–14470 (2012). <https://doi.org/10.1021/jp303844t>
57. K. Kuang, W.K. Chow, X. Ni, D. Yang, W. Zeng, G. Liao, *Fire Mater.* **35**, 353–366 (2011). <https://doi.org/10.1002/fam.1058>
58. R.L. Lehman, J.S. Gentry, N.G. Glumac, *Thermochim. Acta* **316**, 1–9 (1998). [https://doi.org/10.1016/S0040-6031\(98\)00289-5](https://doi.org/10.1016/S0040-6031(98)00289-5)
59. A.E. Newkirk, I. Aliferis, *Anal. Chem.* **30**, 982–984 (1958). <https://doi.org/10.1021/ac60137a031>
60. G.L. Messing, G.Y. Onoda Jr., *J. Am. Ceram. Soc.* **64**, 468–472 (1981). <https://doi.org/10.1111/j.1151-2916.1981.tb09899.x>
61. C. Jiten, M. Rawat, A. Bhattacharya, K.C. Singh, *Mater. Res. Bull.* **90**, 162–169 (2017). <https://doi.org/10.1016/j.materresbull.2017.02.031>
62. R. Singh, P.K. Patro, A.R. Kulkarni, C.S. Harendranath, *Ceram. Int.* **40**, 10641–10647 (2014). <https://doi.org/10.1016/j.ceramint.2014.03.047>
63. J. Pavlič, B. Malič, T. Rojac, *J. Eur. Ceram. Soc.* **34**, 285–295 (2014). <https://doi.org/10.1016/j.jeurceramsoc.2013.09.001>
64. R. Zuo, J. Rödel, R. Chen, L. Li, *J. Am. Ceram. Soc.* **89**, 2010–2015 (2006). <https://doi.org/10.1111/j.1551-2916.2006.00991.x>

Publisher's Note Springer Nature remains neutral with regard to jurisdictional claims in published maps and institutional affiliations.